ROYAL SOCIETY
OF CHEMISTRY

Check for updates

Limiting voltage and capacity fade of lithium-rich, low cobalt $Li_{1.2}Ni_{0.13}Mn_{0.54}Fe_{0.1}Co_{0.03}O_2$ by controlling the upper cut-off voltage

Nabil El Halya, Mohamed Kerroumi, El Houcine Elmaataouy, [ID] Amina Amarray, Mohamed Aqil, Jones Alami and Mouad Dahbi [ID] *

A new $Li_{1.2}Ni_{0.13}Mn_{0.54}Fe_{0.1}Co_{0.03}O_2$ material with a higher content of Fe and lower content of Co was designed *via* a simple sol–gel method. Moreover, the effect of upper cut-off voltage on the structural stability, capacity and voltage retention was studied. The $Li_{1.2}Ni_{0.13}Mn_{0.54}Fe_{0.1}Co_{0.03}O_2$ electrode delivers a discharge capacity of 250 mA h g^{-1} with good capacity retention and coulombic efficiency at 4.6 V cut-off voltage. Importantly, improved voltage retention of 94% was achieved. *Ex situ* XRD and Raman proved that the electrodes cycled at 4.8 V cut-off voltage showed huge structural conversion from layered-to-spinel explaining the poor capacity and voltage retention at this cut-off voltage. In addition, *ex situ* FT-IR demonstrates that the upper cut-off voltage of 4.8 V exhibits a higher intensity of SEI-related peaks than 4.6 V, suggesting that reducing the upper cut-off voltage can inhibit the growth of the SEI layer. In addition, when the $Li_{1.2}Ni_{0.13}Mn_{0.54}Fe_{0.1}Co_{0.03}O_2$ cathode was paired with a synthesized phosphorus-doped TiO_2 anode (P-doped TiO_2) in a complete battery cell, it exhibits good capacity and cycling stability at 1C rate. The material developed in this study represents a promising approach for designing high-performance Li-rich, low cobalt cathodes for next-generation lithium-ion batteries.

Introduction

In recent years, lithium-ion batteries have been widely applied in portable electronic devices such as cellular phones, laptops, and power tools due to their high energy density, low self-discharge, and tiny memory effect.[1–3] However, $LiCoO_2$, the first commercially available cathode material, is plagued by high costs, toxicity, and safety concerns. Other similar layered structure materials, such as $LiNiO_2$, $LiMnO_2$, and $LiMn_2O_4$ have been extensively studied as prospective cathode materials.[4–6] Nevertheless, several problems must be addressed. The synthesis of $LiNiO_2$ has been found to be challenging, and its capacity decreases rapidly due to the formation of the NiO_2 phase.[7–9] Moreover, at higher temperatures, the exothermic decomposition of $LiNiO_2$ in the charged state causes safety issues. In addition, $LiMnO_2$ is thermodynamically unstable and tends to convert rapidly to $LiMn_2O_4$ during cycling.[10,11] $LiMn_2O_4$ also suffers from severe capacity fading at high temperatures due to the Jahn-Teller distortion of Mn^{3+}, Mn ions' dissolution in electrolyte and the formation of two cubic phases and growth of microstrain.[10,12,13] One of the most common alternatives has been lithium nickel cobalt manganese oxides $Li(NiMnCo)O_2$ (NMC) due to their relative low cost, high capacity, and better thermal stability.[14] However, $Li(NiMnCo)O_2$ has inherent

disadvantages such as cation mixing, toxicity and high-capacity losses in the first discharge cycles.[15,16] Therefore, the development of low-cost, non-toxic, and high-capacity cathode materials is needed. To improve the structural stability and the electrochemical performance of $Li(NiMnCo)O_2$ based materials, various metal doping such as Al, Cr, Fe, Mo, Mg, Zr, and Si has been studied.[17–22]

Recently, Layered lithium-rich NMC (Li-rich NMC) has been extensively studied due to its enhanced performances, especially the high discharge capacity (>250 mA h g^{-1}).[23–30] However, Li-rich NMC cathodes still suffer from serious drawbacks such as the poor rate capabilities and the non-stable electrochemical performances (capacity and voltage fading) caused by the transition metals leaching during cycling and the crystal structures changes. Besides, there is the degradation of the different components of the electrodes such as the binder, conductive additive, and the electrolyte. Several strategies have been adopted to stabilize the crystal structure and decrease the voltage and capacity drop of Li-rich NMC cathode material including surface coating,[31–36] doping,[29,37–45] structural modification,[46–53] lithium extraction,[54–57] and electrolyte modification.[58–64]

Controlling the cut-off voltage can be also an effective strategy for stabilizing the crystal structure and decreasing the capacity and voltage drop of Li-rich NMC cathode materials.[65–70] The conventional cycling protocol typically extends the upper cut-off voltage to 4.8 V to achieve higher capacities, however this

Materials Science and Nano-engineering Department, Mohammed VI Polytechnic University, Ben Guerir, Morocco. E-mail: Mouad.dahbi@um6p.ma

causes huge structural instability and voltage drop. By setting the upper cut-off voltage to a lower value, the material is not fully charged and remains partially discharged, which can help to stabilize the crystal structure and reduce the voltage drop. This is because the material can maintain a higher average oxidation state, which can reduce the formation of unwanted side reactions and increase the overall stability of the material.[67,69,70]

Here, a new Li-rich $Li_{1.2}Mn_{0.54}Ni_{0.13}Fe_{0.1}Co_{0.03}O_2$ (NMCF) cathode material with higher content of Fe and lower content of Co was prepared *via* a simple sol–gel method. Moreover, the effect of upper cut-off voltage on the capacity and voltage retention of NMCF during charge/discharge cycling was identified. According to our findings, NMCF electrodes undergo phase changes at high charge voltage (4.8 V). Nonetheless, the electrode cycled at a moderate voltage range of 4.6 V displayed enhanced structural stability, as well as low capacity and voltage fading during repeated cycling. By restricting the upper cut-off voltage to lower values, the present study aims to limit the structural rearrangements that cause the capacity and voltage fade and ensure more cycling stability during prolonged charge/discharge cycling.

Experimental

Synthesis of NMCF material

NMCF material was synthesized using a simple sol–gel route. Stoichiometric amount of $LiCH_3COO\cdot2H_2O$ (with an excess of 5 wt%) (99% Sigma Aldrich), $C_4H_6MnO_4\cdot4H_2O$ (99% Sigma Aldrich), $C_4H_6NiO_4\cdot4H_2O$ (99% Sigma Aldrich), $C_4H_6CoO_4\cdot4H_2O$ (99% Sigma Aldrich), and $FeC_2O_4\cdot2H_2O$ (99% Sigma Aldrich), were mixed in distilled water with citric acid ($C_6H_8O_7$, 99% Sigma Aldrich), as a chelating agent (molar ratio of citric acid to total metal ions is 1 : 1.2). The pH of the solution was adjusted to 9 using a solution of 0.2 M ammonia. Subsequently, the solution was placed in a water bath at 80 °C and stirred until the formation of a wet gel. The gel was further dried overnight at 120 °C, ground and then calcined at 850 °C for 5 h in an air atmosphere to obtain $Li_{1.2}Mn_{0.54}Ni_{0.13}Fe_{0.1}Co_{0.03}O_2$ powder.

Electrochemical measurements

NMCF electrodes were prepared by mixing 85% wt of active material, 10% wt of carbon black (Sigma Aldrich) and 5% wt of PVDF (Sigma Aldrich) binder. The mixture was dissolved in *N*-methyl-2-pyrrolidone (NMP, 99.5%, Sigma Aldrich) and casted onto Al current collector using doctor blade. The casting was air dried in oven at 70 °C and punched into circular disks. The coin cells were assembled in an Ar-filled glovebox using lithium foil as counter electrodes, WHATMAN glass microfiber filter as separator and 1 M $LiPF_6$ in EC : DMC (1 : 1) as electrolyte. For Full Cell measurement, P-doped TiO_2 (synthesis process and electrochemical performances are details in our recent studies[71,72]) was used as negative electrode. This electrode was composed of 85% wt of P-doped TiO_2 active material, 10% wt of carbon black, and 5% wt PVDF. The N/P mass ratio was about 1.12. A dis/charge rate of 1C was applied, which corresponds to a specific current of 200 mA g^{-1} for the positive electrode material.

Materials characterizations

The synthesized samples were characterized by a powder X-ray diffractometer (Bruker D8 Advance powder) using an incident X-ray beam coming from a copper anticathode with a wavelength $\lambda = 1.54060$ Å of Kα1 and $\lambda 2 = 1.54439$ Å of Kα2. The samples' morphology and structure were recorded by a field emission scanning electron microscope (ZEISS EVO (SEM) from Carl Zeiss Microscopy) and high-resolution Raman microscopes (Lab RAM HR Evolution Raman microscopes). Chemical bonding of NMCF electrodes after cycling were identified using Fourier transform infrared spectroscopy (FTIR, PerkinElmer Spectrometer). For the electrochemical measurements, cyclic voltammetry at different scan rates, charge–discharge tests, and electrochemical impedance spectroscopy (form 100 kHz to 10 mHz) were performed using a biologic battery tester within two potential window 2.5–4.6 V and 2.5–4.8 V.

Results and discussion

NMCF powder was characterized by X-ray diffraction as shown in Fig. 1a, followed by Rietveld refinement. All diffraction peaks can be indexed to a typical hexagonal–NaFeO$_2$ layered structure with $R\bar{3}m$ space group, except the weak peaks at around $2\theta = 20$–25° which are attributed to the Li_2MnO_3 component (monoclinic structure with space group $C2/m$). These diffractions are relevant to the LiM_6 cation ordering that occurs in the transition metal layers of Li_2MnO_3. The reliability factors (R_p (%): 8.65, R_{wp} (%): 9.21, R_{exp} (%): 10.34 and χ^2: 1.02) provide strong evidence that both structural types align effectively with the peaks in the calculated pattern and are in excellent agreement with the observed data. Other impurity peaks were not observed, indicating that the material was successfully synthesized with better crystallinity and pure phase content. Furthermore, the $I_{(003)}/I_{(104)}$ ratio was 1.3, which indicates that the materials have excellent cation ordering (low amount of Li$^+$ and Ni^{2+} disordering). Tables 1 and 2 provide the structural parameters of Li_2MnO_3 and $LiNi_{0.13}Mn_{0.54}Fe_{0.1}Co_{0.03}O_2$, which together form the material NMCF. The parameters were compared to those of other Li-rich layered materials with similar stoichiometry that have been previously reported in literature.

The Raman spectra are presented in Fig. 1b. The two significant Raman bands appearing at around 594 and 474 cm^{-1} in the spectra results from the stretching A$_{1g}$ modes (originate from the O–M–O bending vibrations) and bending E$_g$ (originate from the M–O symmetrical stretching), respectively. An additional small Raman band at 424 cm^{-1} could be attributed to the monoclinic Li_2MnO_3 phase. This result proves that the prepared material has an excellent layered structure with a $R\bar{3}m$ symmetry.[75]

Scanning Electron Microscopy (SEM) images of NMCF samples with different magnification levels are shown in Fig. 2a. The NMCF powder appear as homogeneous round-like particles with submicron-size in the range of 150–400 nm. This
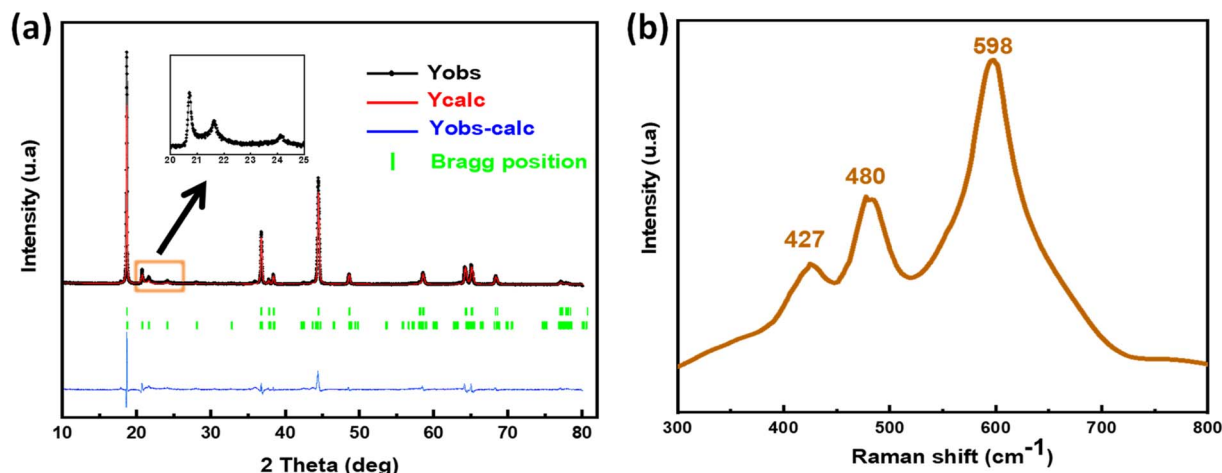
Fig. 1 XRD pattern (a) and Raman spectra (b) of NMCF material.

Table 1 Structural parameters obtained from Rietveld refinement of XRD of the phase Li_2MnO_3

Structure	a (Å)	b (Å)	c (Å)	β (°)	Ref.
$Li_{1.2}Mn_{0.54}Ni_{0.13}Fe_{0.1}Co_{0.03}O_2$	4.9498	8.5448	5.0342	109.264	This work
$Li_{1.2}Mn_{0.56}Ni_{0.16}Co_{0.08}O_2$	4.9529	8.5538	5.0311	109.246	31
$Li_{1.2}Mn_{0.56}Ni_{0.13}Co_{0.13}O_2$	4.9540	8.5153	5.0094	108.880	73

Table 2 Structural parameters of $Li_{1.2}Mn_{0.54}Ni_{0.14}Fe_{0.1}Co_{0.03}O_2$ compared to the literature

Structure	a (Å)	b (Å)	c (Å)	c/a	Ref.
$Li_{1.2}Mn_{0.54}Ni_{0.13}Fe_{0.1}Co_{0.03}O_2$	2.863	2.863	14.277	4.986	This work
$Li_{1.2}Mn_{0.56}Ni_{0.16}Co_{0.08}O_2$	2.866	2.866	14.304	4.990	74

morphology shortens the migration paths of Li ions by offering an adequate contact between the material and electrolyte. Fig. 2b and c shows the Energy-Dispersive X-ray (EDX) elemental mapping analysis and the EDX spectrum of NMCF material. The sample contains Ni, Co, Mn, Fe and O elements with no other impurities. Moreover, Mn, Co, Ni, Fe, and O atoms are uniformly distributed on the surface of NMCF powder.

Fig. 3a depicts the initial charge–discharge curves of NMCF electrodes at a current density of 0.1C rate ($1C = 200$ mA g^{-1}) within the voltage ranges of 2.0–4.6 V and 2.0–4.8 V. Both charge curves exhibit the features of layered Li-rich cathodes. The slope observed at 4.5 V is attributed to the process of lithium disinsertion from the $LiMn_xNi_yFe_zCo_{1-x-y-z}O_2$ component of $Li_{1.2}Mn_{0.54}Ni_{0.13}$-$Fe_{0.1}Co_{0.03}O_2$, along with the oxidation of Ni^{2+} to Ni^{4+} and Co^{3+} to Co^{4+}. The plateau observed at 4.5 V is due to the activation of the Li_2MnO_3 phase and the extraction of Li_2O, which result in irreversible capacity loss. Moreover, compared to the electrode cycled under a cut-off voltage of 4.6 V, the electrode cycled under 4.8 V exhibits a higher discharge capacity of 220.5 mA h g^{-1} due to its fast activation in the initial charge process.

Cyclic voltammetry test of NMCF electrode was carried out within the voltage range of 2.5–4.8 V at 0.1 mV s^{-1} scan rates to evaluate the redox potential of metal ions (Fig. 3b). The strong anodic peak at 4.6 V is attributed to the activation reaction of Li_2MnO_3 that lead to oxygen release and remove Li_2O from the Li_2MnO_3 component. This reaction disappears in the subsequent cycles. In addition, the anodic peak at 4.2 V corresponds to the oxidation reaction of Co^{3+}, Fe^{3+} and Ni^{2+} ions to Co^{4+}, Fe^{4+} and Ni^{4+}.[76] The cathodic peaks at ~3.8 V, ~2.8 V are due to the reduction of $Ni^{4+}/Fe^{4+}/Co^{4+}$ to $Ni^{2+}/Fe^{3+}/Co^{3+}$ and Mn^{4+} to Mn^{3+}, respectively.[77] Furthermore, cyclic voltammetry multi-rate was carried out to calculate the lithium-ions diffusion coefficient using the Randles–Sevcik equation:

$$I_p = 2.69 \times 10^5 A n^{3/2} C_0 D^{1/2} v^{1/2}$$

where I_p is the peak current (mA), A is the electrode surface area (cm^2), n is the number of exchanged electrons (for Li$^+$ it is 1), C_0 is the molar concentration of Li$^+$ in the NMCF, D is the diffusion coefficient (cm^2 s^{-1}) and v is the scan rate (mV s^{-1}).

According to the results displayed in Fig. 3c and d, the calculated anodic and cathodic diffusion coefficients of NMCF electrode are 1.57, and 3.25 ($\times 10^{-11}$ cm^2 s^{-1}), respectively. The obtained values agree with those reported in previous studies on the most advanced lithium-rich cathodes.[78] This agreement suggests that the obtained results could lead to improved electrochemical performance.

The Li-rich materials are well known in the literature by their structural conversion from layered to spinel that occurs during prolonged cycling. This phenomenon results in a huge capacity and voltage fading.[74,75] To clearly show this phase evolution during prolonged cycling, charge/discharge profiles and their
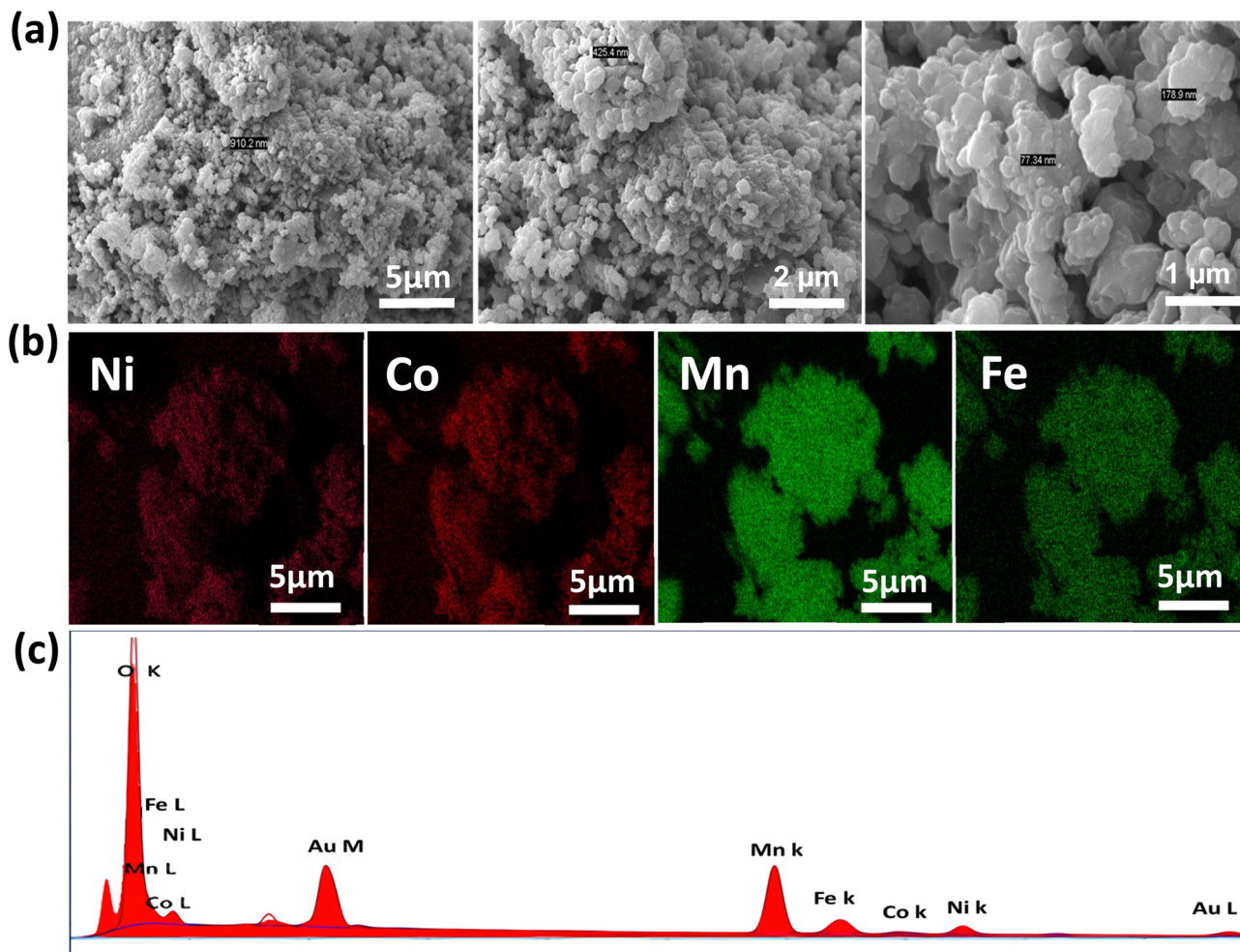
Fig. 2   SEM images (a), Energy–Dispersive X-ray (EDX) elemental mapping analysis (b), EDX spectrum of NMCF material (c).

differential capacity plots for 4.8 and 4.6 V cut-off voltages were plotted (Fig. 4a–d). Under both cut-off voltages, the NMCF electrode shows a peak at 3.3 V which is attributed to the reduction of Mn^{4+} to Mn^{3+}. However, at 4.8 V cut-off voltage this peak shift to lower potentials after 100 cycles and a new peak appears at 2.8 V suggesting the formation of the spinel phase. More importantly, at 4.6 V, the peak corresponding to the spinel phase was not observed after 100 cycles expect the low shift to lower potentials which can be explained by the modification of the layered structure.[79] Fig. 4e presents a comparison of the average discharge voltages at the cut-off voltages of 4.6 V and 4.8 V. Notably, the discharge average voltage at the 4.6 V cut-off voltage is observed to be higher than that at the 4.8 V cut-off voltage. Furthermore, after 100 cycles, the decrease in discharge voltage is significantly lower when the 4.6 V cut-off voltage is applied (94%) in contrast to the 4.8 V cut-off voltage (90%).

Fig. 5a displays the cycling performances and coulombic efficiencies of NMCF electrode cycled under 4.6 V and 4.8 V cut-off voltages to evaluate their galvanostatic charge/discharge properties. At C/10 rate, both electrodes exhibit two contrasting developing trends in terms of cycling performance. As the

cycling progresses, the specific capacity of the electrode cycled under a cut-off voltage of 4.6 V gradually increases, with an initial discharge specific capacity of only 183.8 mA h g^{-1}. Similarly, the specific capacity of the electrode cycled under 4.8 V cut-off voltage shows an increasing trend in the initial cycles, and after 10 cycles, a maximum discharge specific capacity of 289.2 mA h g^{-1} was achieved, which is closely associated with the gradual activation of the redox reaction. Moreover, under 4.6 V cut-off voltage a better cycling stability was achieved. Despite having a lower first discharge specific capacity of 183.8 mA h g^{-1}, the electrode cycled under a cut-off voltage of 4.6 V exhibits higher cycling stability. Notably, compared to previous reports of Fe-based Li-rich materials,[80–82] NMCF material displays a significantly higher discharge capacity of 238.6 mA h g^{-1} after 100 cycles. Moreover, due to the good capacity and voltage stability under the cut-off voltage of 4.6 V, NMCF electrode delivers an energy retention of 89% after 100 cycles at C/10 (Fig. 5b).

The rate capability of NMCF cathode under 4.6 V and 4.8 V cut-off voltages is shown in Fig. 6a. The NMCF electrodes display comparable reversible capacities under both cut-off voltages. Nevertheless, a lower discharge capacity was
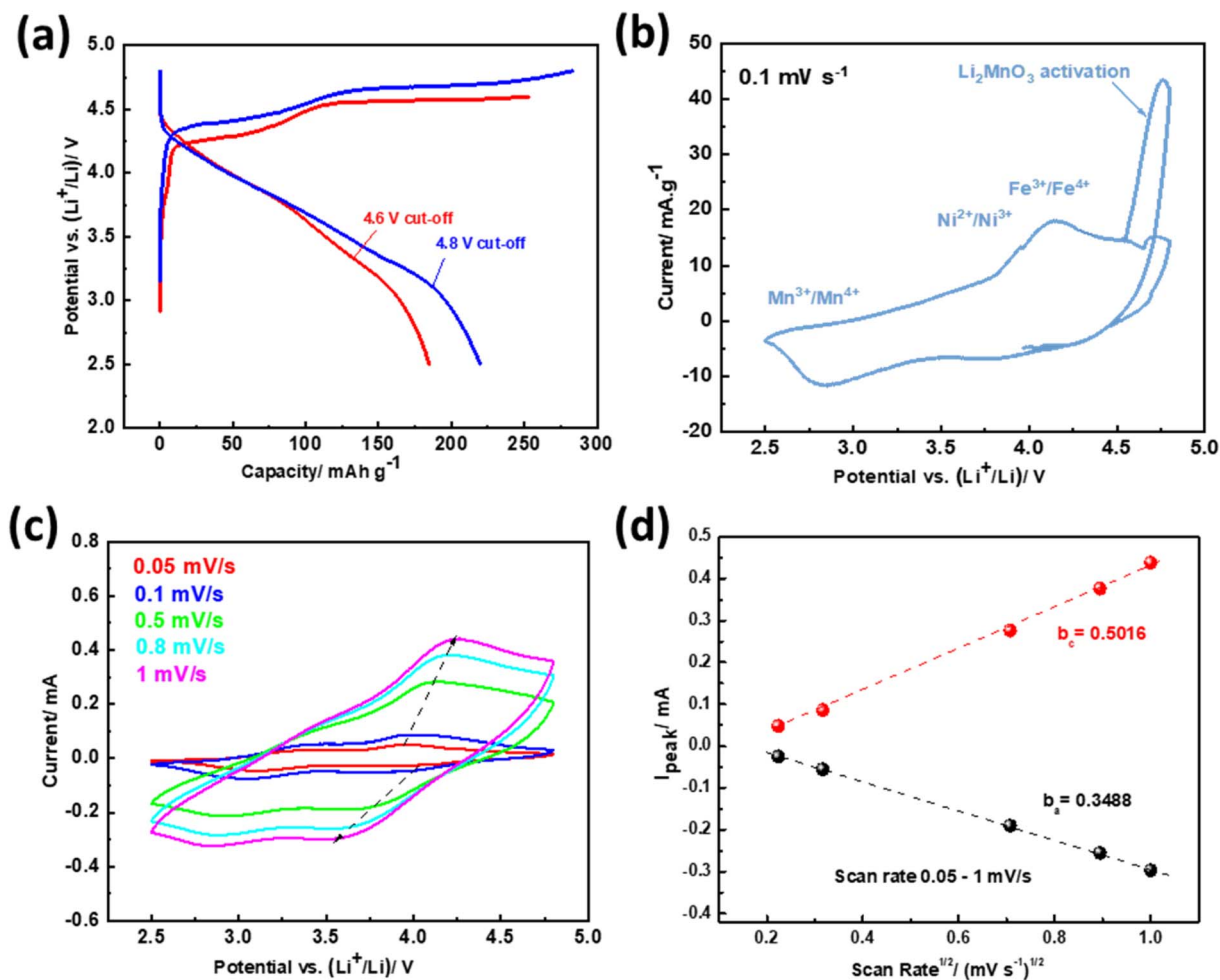
Fig. 3 First charge/discharge profiles cycled at C/10 under the cut-off voltages of 4.6 and 4.8 V (a), cyclic voltammogram of the first cycle scanned at 0.1 mV s^{-1} (b), cyclic voltammetry curves at different scan rates (c), anodic and cathodic peak current *versus* square root of scane rate of NMCF electrodes (d).

obtained for the electrode cycled under 4.8 V cut-off voltage when the rate recovers to C/10, indicating the low structural stability and the poor performance of the electrode cycled under a cut-off voltage of 4.8 V after high-rate cycling. These results prove that maintaining a cut-off voltage of 4.6 V is crucial for achieving stable capacity and voltage, as well as high-rate capability of NMCF cathode.

Electrochemical impedance spectroscopy (EIS) was used in a frequency range from 10 mHz to 10 MHz at room temperature in the discharged state ±2.5 to follow the evolution of charge transfer resistance during cycling (Fig. 6b). The widening of the semicircle observed at the cut-off 4.8 V, indicates that NMCF electrode has undergone accumulated severe defects. Jotti Karunawan *et al.* have attributed the increased charge transfer resistance to the cracks formation as well as the structural evolution from layered to spinel or rock salt.[83] These results explain the poor electrochemical performance for the electrode cycled at 4.8 V.

To identify the effect of upper cut-off voltage on the structural stability of NMCF material upon cycling *ex situ* XRD was carried out. The XRD patterns of non-cycled and cycled electrodes at C/10 under 4.6 V and 4.8 V cut-off voltages are shown in Fig. 7a. After 100 cycles, the (003), (018) and (113) peaks become broader and weaker for both cut-off voltages indicating a decrease of the material crystallinity.[84] Moreover, the two electrodes exhibit a noticeable shift towards lower 2θ angles of the most intense (003) reflection after cycling. This shift is also observed in other reflections, suggesting a lattice expansion along the *c*-axis. The increased repulsion of the transition metal layers caused by the irreversible loss of lithium after activation is the reason for this expansion. The (110) and (020) reflections, which are attributed to the Li_2MnO_3 phase, have disappeared after 100 cycles in both cut-off voltages which confirms the charge/discharge results. Furthermore, the $I_{(003)}$/$I_{(104)}$ ratio after 100 cycles at C/10 was 1.01 for the electrode cycled under 4.6 V cut-off voltage compared to 0.90 for the electrode cycled under 4.8 V, which indicates that a large amount of transition-metal ions immigrate into the Li layers under 4.8 V cut-off voltage. In addition, the peak at 43.6° indicated the formation of the spinel structure. This peak is more intense for the electrode cycled under 4.8 V cut-off voltage. The obtained result proves that the cut-off voltage can be the major
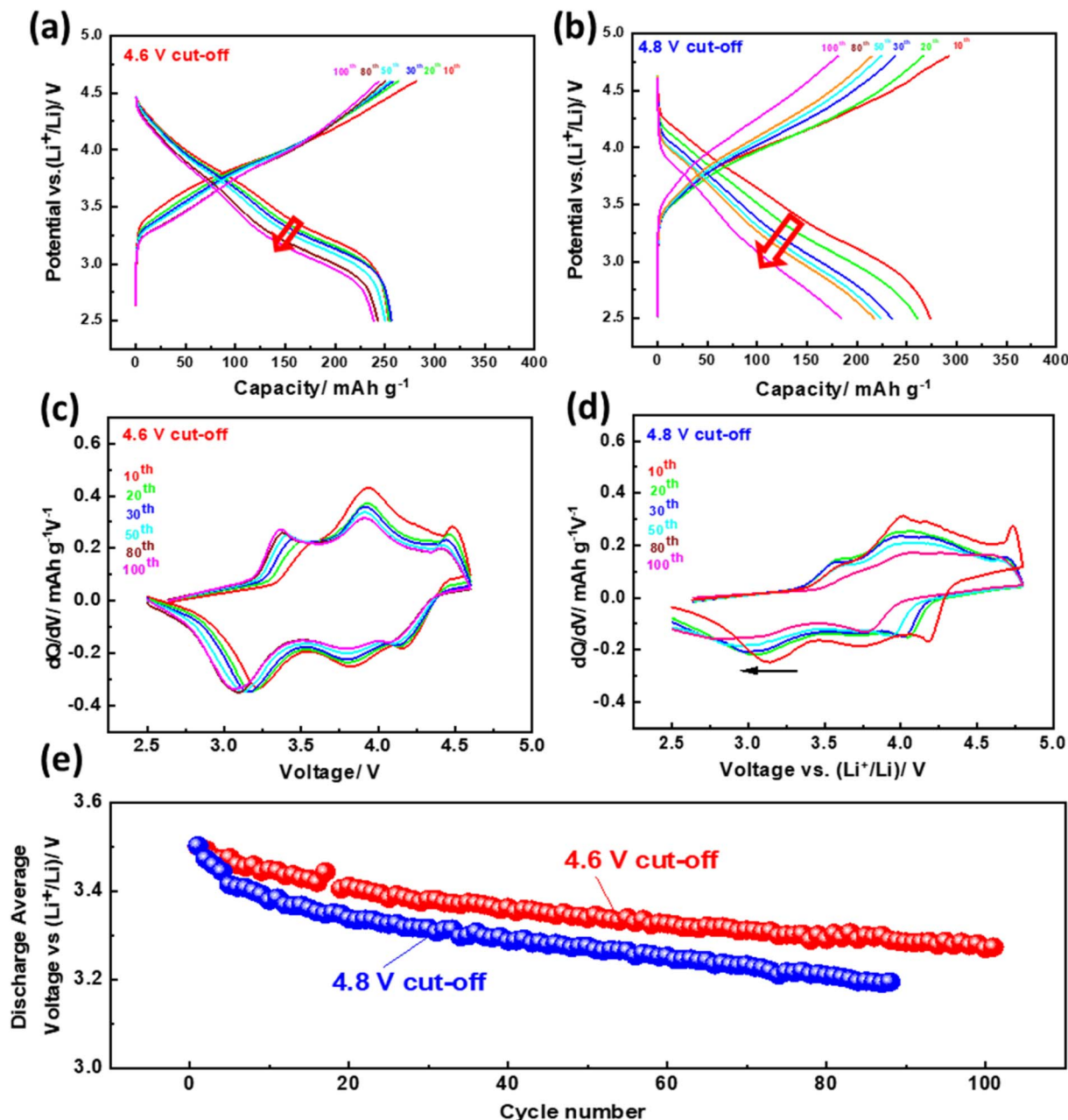
Fig. 4 Galvanostatic discharge/charge curves (a and b), dQ/dV plots (c and d), discharge average voltage (e) of NMCF electrode cycled at C/10 under the cut-off voltages of 4.6 and 4.8 V.

factor that control the structural stability of NMCF materials. In addition *ex situ* Raman spectroscopy was carried out to follow the structural evolution of NMCF cathode during cycling. Fig. 7b compares the Raman spectra of the non-cycled and cycled electrodes under 4.6 V and 4.8 V cut-off voltages after 100 cycles. The first Raman band at 423 cm^{-1} related to the Li_2MnO_3 phase is completely disappeared after cycling for both cut-off voltages which prove the result obtained by *ex situ* XRD. The other two Raman bands are shifted to higher values with significant decrease in the integral intensities indicating the structural changes upon cycling. These changes are clearer for the electrode cycled at 4.8 V comparing to 4.6 V. Thus, working

at 4.6 V may suppress the phase transition observed for lithium-rich materials during cycling.

The effect of upper cut-off voltage on SEI formation was further examined using *ex situ* FTIR spectroscopy (Fig. 8). After 100 cycles, NMCF electrodes cycled at both upper cut-off voltages exhibit new absorption peaks in their FTIR spectra, which are attributed to SEI species present in the SEI layer. The SEI layer is composed of common species such as Li_2CO_3, $ROCO_2Li$ (lithium alkyl carbonate), and $Li_xPO_yF_z$ (species containing fluoride and phosphate).[85] It is important to note that non-cycled electrodes do not come in contact with electrolyte, and thus do not form the SEI layer on their surface. The peak at
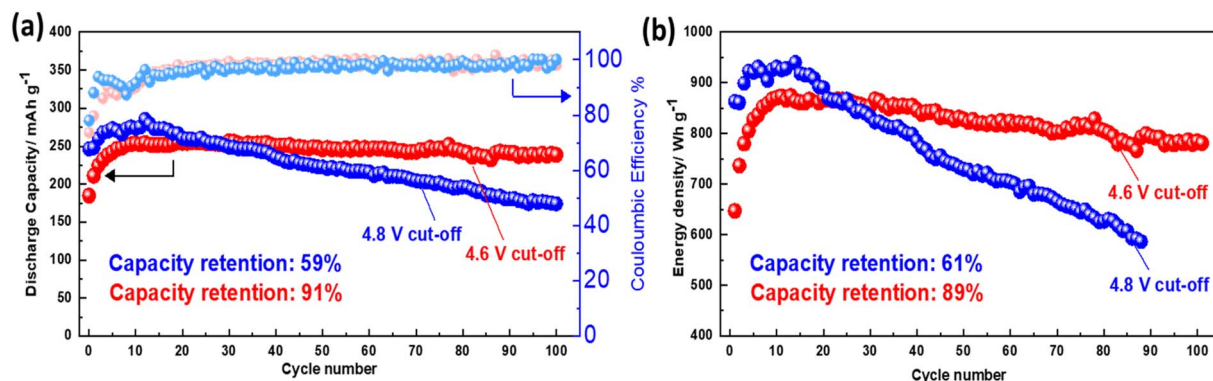
Fig. 5 Cycling performance and coulombic efficiency (a), calculated energy density (b) of NMCF electrodes cycled at C/10 under the cut-off voltages of 4.6 and 4.8 V.
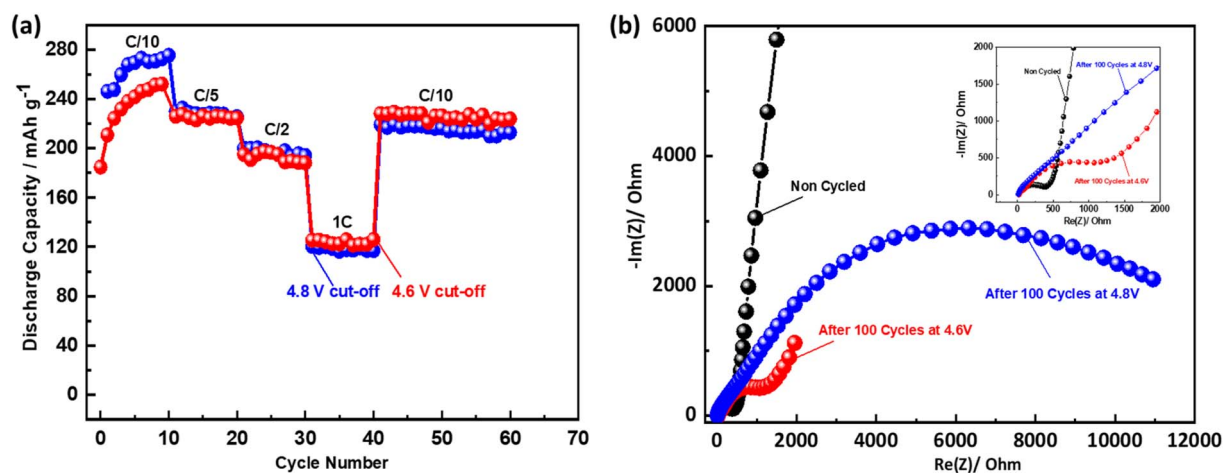

Fig. 6 Rate capability of NMCF electrodes at variant current rates from C/10 to 1C (1C = 200 mA g^{-1}) under the cut-off voltages of 4.6 V and 4.8 V (a), Nyquist plot (b) and the equivalent circuit model (c) of NMCF electrodes after 100 cycles at C/10 under the cut-off voltages of 4.6 and 4.8 V.

875 cm^{-1} is present in all samples and is attributed to Li_2CO_3 impurity produced from the reaction between unreacted lithium salt and carbon dioxide on the surface of NMCF particles.[86,87] The peak at 1412 cm^{-1} is assigned to the vibration of CO_3^{2-}.[87] Li_2CO_3 is one of the main SEI components formed on the surface of high voltage cathode materials during cycling.

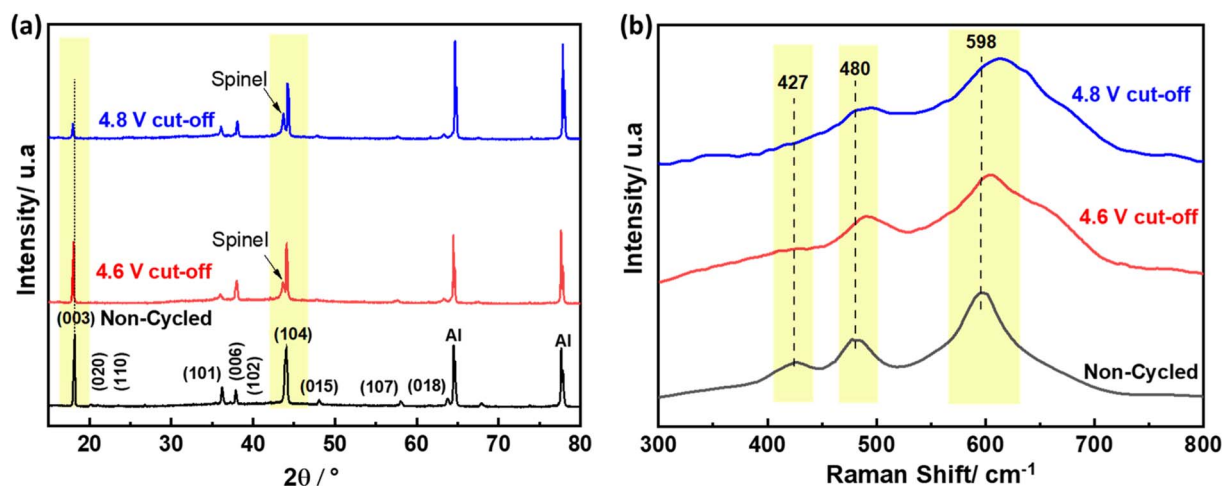**Fig. 7** *Ex situ* XRD (a) and *ex situ* Raman (b) of NMCF electrodes after 100 cycles at C/10 under the cut-off voltages 4.6 V and 4.8 V.
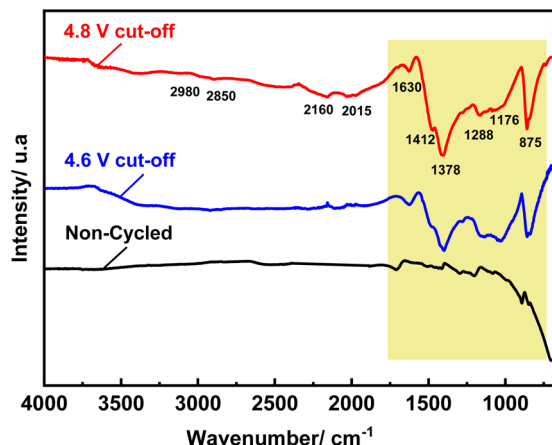
Fig. 8 *Ex situ* FT-IR of NMCF electrodes after 100 cycles at C/10 under the cut-off voltages of 4.6 V and 4.8 V.

The C–H vibration peaks of $ROCO_2Li$ can be seen at 2850 and 2935 cm^{-1}.[88] Additionally, the vibration of COO^- and $C=O$ bindings related to $ROCO_2Li$ are observed at 1378 and 1630 cm^{-1}, respectively. The Li–F vibrations of $Li_xPO_yF_z$ can be observed at 1176 and 1288 cm^{-1}.[87] These results demonstrate that the cycled NMCF electrode at an upper cut-off voltage of 4.8 V exhibits a higher intensity of SEI-related peaks than that cycled at 4.6 V which agrees with the result obtained from

electrochemical impedance spectroscopy. Overall, reducing the upper cut-off voltage can inhibit the growth of the SEI layer resulting in a lower charge transfer resistance.

Finally, to evaluate the performance of NMCF material in a complete battery system, a full cell using P-doped TiO_2 anode was designed (Fig. 9a). P-doped TiO_2 has shown excellent first coulombic efficiency, lithium-ion diffusion, and capacity retention during prolonged cycling.[72] The output voltage of the full cell was 2.3 V which match the voltage difference between P-doped TiO_2 and NMCF. Moreover, Fig. 9b illustrates the charge/discharge cycles of the full cell at 1C current rate within the voltage window of 1–3.5 V. During the first cycle, the full cell exhibited a capacity of 130 mA h g^{-1}, which is based on the mass of NMCF cathode. The cycling performance of the full cell (shown in Fig. 9c) was further investigated. After 70 cycles, a capacity retention of 87% was achieved at 1C. Additionally, the coulombic efficiency was observed to be 100%. The low capacity of NMCF electrode in the full cell is mainly due to its low first coulombic efficiency which does not exceed 70%. This low first coulombic efficiency of NMCF cathode could be attributed to several factors, including the decomposition of the electrolyte, the formation of a thick SEI layer, and the dissolution of transition metal ions from the cathode material. To overcome these issues, further works must be carried out, such as modifying the electrolyte composition, optimizing the electrode microstructure, and coating the NMCF cathode material with protective layers.

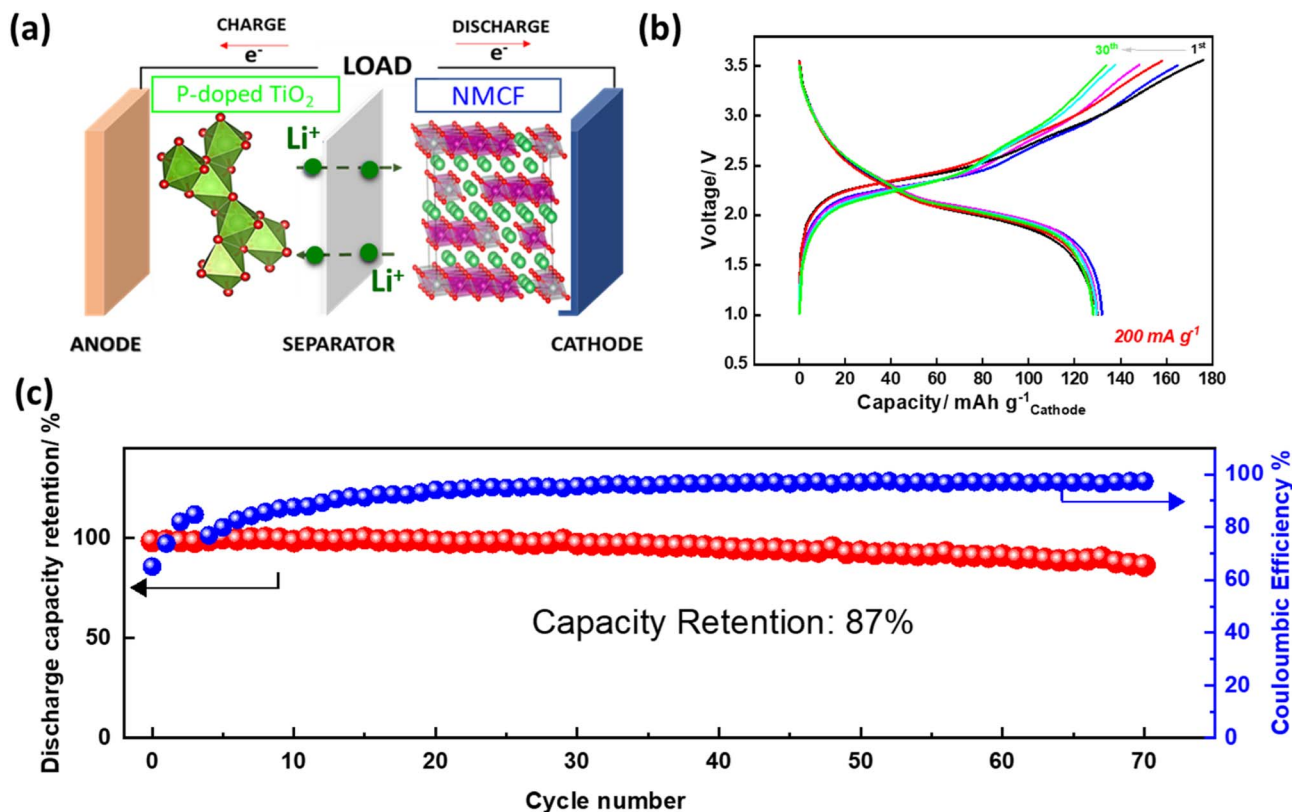Fig. 9 Schematic illustration of the P-doped TiO_2/NMCF full cell (a), charge/discharge cycle of the full cell performed at 1C rate (1C = 200 mA g^{-1}) within the voltage range 1–3.5 V (b), cycling performances at 1C charge/discharge rate (c).

Conclusions

In summary, the present study was carried out to determine the effect of upper cut-off voltage on the structure stability, capacity retention and voltage retention of NMCF cathode material. This material was successfully synthesized by a simple sol–gel method. In addition, as confirmed by XRD Rietveld refinement, the prepared material has a hexagonal–$NaFeO_2$ layered structure with excellent cation mixing. Besides, at 0.1C current rate, the electrode delivers good capacity retention and coulombic efficiency when using an upper cut-off voltage of 4.6 V. Importantly, a discharge voltage retention of 94% was obtained at this cut-off voltage. *Ex situ* XRD and Raman of the electrode cycled at C/10 were proved that the spinel phase occurs at both cut-off voltages, but is not dominant in 4.6 V. Besides *ex situ* FT-IR demonstrates that the upper cut-off voltage of 4.8 V exhibits a higher intensity of SEI-related peaks than 4.6 V, suggesting that reducing the upper cut-off voltage can inhibit the growth of the SEI layer and the surface corrosion of NMCF particles. Finally, NMCF cathode material was evaluated in a full cell using P-doped TiO_2 anode. The output voltage of the full cell was 2.3 V with acceptable first capacity and capacity retention. The low capacity of NMCF electrode in the Full cell is mainly due to its low first coulombic efficiency which does not exceed 70%. The benefits of lithium-rich cathodes, including their high energy density, improved thermal stability, and lower cost, make them an attractive option for the future of battery technology. However, further research and development are needed to improve their first coulombic efficiency and overall performance.

Author contributions

Nabil El Halya: idea conception, experimental investigation and writing of the original draft. Mohammed Kerroumi: formal analysis, experimental part, ElHoucine Elmaataouy: XRD measurement and Rietveld refinement, Amina Amarray: review and editing, Mouad Dahbi and Jones Alami: conceptualization, validation, review & editing, funding acquisition.

Conflicts of interest

The authors declare that they have no known competing financial interests or personal relationships that could have appeared to influence the work reported in this paper.

Acknowledgements

References

1 Z. Guo, L. Li, Z. Su, G. Peng, M. Qu, Y. Fu, H. Wang and W. Ge, *Electrochim. Acta*, 2023, **437**, 141525.

2 J. Liu, H. Yuan, X. Tao, Y. Liang, S. J. Yang, J. Huang, T. Yuan, M. Titirici and Q. Zhang, *EcoMat*, 2020, **2**(1), e12019.

3 R. Razaq, N. Zhang, Y. Xin, Q. Li, J. Wang and Z. Zhang, *EcoMat*, 2020, **2**(2), e12020.

4 R. Pan, E. Jo, Z. Cui and A. Manthiram, *Adv. Funct. Mater.*, 2023, **33**, 2211461.

5 X. Hou, X. Liu, H. Wang, X. Zhang, J. Zhou and M. Wang, *Energy Storage Mater.*, 2023, **57**, 577–606.

6 X. Zhu, F. Meng, Q. Zhang, L. Xue, H. Zhu, S. Lan, Q. Liu, J. Zhao, Y. Zhuang, Q. Guo, B. Liu, L. Gu, X. Lu, Y. Ren and H. Xia, *Nat. Sustainability*, 2020, **4**, 392–401.

7 M. Bianchini, F. Fauth, P. Hartmann, T. Brezesinski and J. Janek, *J. Mater. Chem. A*, 2020, **8**, 1808–1820.

8 E. Bautista Quisbert, F. Fauth, A. M. Abakumov, M. Blangero, M. Guignard and C. Delmas, *Small*, 2023, 2300616.

9 S. Ober, A. Mesnier and A. Manthiram, *ACS Appl. Mater. Interfaces*, 2023, **15**, 1442–1451.

10 G. Hao, Q. Lai and H. Zhang, *J. Energy Chem.*, 2021, **59**, 547–571.

11 H. Zhang, X. Gao, Q. Cai, X. Zhang, Y. Tian, M. Jia, W. Xie, Y. Du and X. Yan, *J. Mater. Chem. A*, 2023, **11**, 8426–8452.

12 S. Zhang, H. Chen, J. Chen, S. Fang, L. Ni, H. Wang, W. Deng, G. Zou, H. Hou and X. Ji, *Adv. Funct. Mater.*, 2023, **33**, 2210731.

13 C.-L. Mu, Y.-X. Qi, W. Liu and Y.-J. Bai, *ACS Appl. Electron. Mater.*, 2023, **5**, 1793–1803.

14 K. H. Chan, H. Liu and G. Azimi, *Ind. Eng. Chem. Res.*, 2023, **62**, 4271–4280.

15 Y. Yoon, S. Shin and M. W. Shin, *ACS Appl. Polym. Mater.*, 2023, **5**, 1344–1353.

16 K. Egorov, W. Zhao, K. Knemeyer, A. N. Filippin, A. Giraldo and C. Battaglia, *ACS Appl. Mater. Interfaces*, 2023, **15**, 20075–20080.

17 A. Hebert, C. David and E. McCalla, *ACS Appl. Energy Mater.*, 2023, **6**, 4593–4603.

18 H. Darjazi, E. Gonzalo, B. Acebedo, R. Cid, M. Zarrabeitia, F. Bonilla, M. Á. Muñoz-Márquez and F. Nobili, *Mater. Today Sustain.*, 2022, **20**, 100236.

19 L. Azhari, B. Sousa, R. Ahmed, R. Wang, Z. Yang, G. Gao, Y. Han and Y. Wang, *ACS Appl. Mater. Interfaces*, 2022, **14**, 46523–46536.

20 H. Qian, H. Ren, Y. Zhang, X. He, W. Li, J. Wang, J. Hu, H. Yang, H. M. K. Sari, Y. Chen and X. Li, *Electrochem. Energy Rev.*, 2022, **5**, 2.

21 X. Wang, H. Zhou, Z. Chen and X. Meng, *Energy Storage Mater.*, 2022, **49**, 181–208.

22 H. Darjazi, S. J. Rezvani, S. Brutti and F. Nobili, *Electrochim. Acta*, 2022, **404**, 139577.

23 P. Vanaphuti, J. Chen, J. Cao, K. Bigham, B. Chen, L. Yang, H. Chen and Y. Wang, *ACS Appl. Mater. Interfaces*, 2019, **11**, 37842–37849.

24 Y. Huang, K. Wu, R. Hao, W. Miao, Y. Cai, P. Wang, J. Cheng, Z. Wang, Q. Li, B. Guo and A. Nie, *ACS Appl. Energy Mater.*, 2021, **4**, 2489–2495.

25 S. Y. Luchkin, M. A. Kirsanova, D. A. Aksyonov, S. A. Lipovskikh, V. A. Nikitina, A. M. Abakumov and K. J. Stevenson, *ACS Appl. Energy Mater.*, 2022, **5**, 7758–7769.

26 A. Celeste, M. Tuccillo, A. Santoni, P. Reale, S. Brutti and L. Silvestri, *ACS Appl. Energy Mater.*, 2021, **4**, 11290–11297.

27 A. V. Morozov, I. A. Moiseev, A. A. Savina, A. O. Boev, D. A. Aksyonov, L. Zhang, P. A. Morozova, V. A. Nikitina, E. M. Pazhetnov, E. J. Berg, S. S. Fedotov, J.-M. Tarascon, E. V. Antipov and A. M. Abakumov, *Chem. Mater.*, 2022, **34**, 6779–6791.

28 D. Bosubabu, K. B. MG and K. Ramesha, *ACS Appl. Energy Mater.*, 2020, **3**, 10872–10881.

29 A. Yalçın, M. Demir, M. O. Güler, M. Gönen and M. Akgün, *Electrochim. Acta*, 2023, **440**, 141743.

30 M. Akhilash, P. S. Salini, B. John, N. Supriya, S. Sujatha and T. D. Mercy, *Ionics*, 2023, **29**, 983–992.

31 U. Nisar, R. Petla, S. A. Jassim Al-Hail, A. A. Quddus, H. Monawwar, A. Shakoor, R. Essehli and R. Amin, *RSC Adv.*, 2020, **10**, 15274–15281.

32 B. Zhao, J. Xie, H. Zhuang, X. Liu, W. Li, X. Hu, Y. Jiang and J. Zhang, *Solid State Ionics*, 2020, **347**, 115245.

33 A. Shevtsov, H. Han, A. Morozov, J. C. Carozza, A. A. Savina, I. Shakhova, N. R. Khasanova, E. V. Antipov, E. V. Dikarev and A. M. Abakumov, *Nanomaterials*, 2020, **10**, 1870.

34 X. Ji, Y. Xu, H. Feng, P. Wang, Y. Zhou, J. Song, Q. Xia and Q. Tan, *ACS Appl. Mater. Interfaces*, 2021, **13**, 47659–47670.

35 N. H. Vu, J. C. Im, S. Unithrattil and W. Bin Im, *J. Mater. Chem. A*, 2018, **6**, 2200–2211.

36 X. Wan, W. Che, D. Zhang and C. Chang, *Mater. Charact.*, 2020, **169**, 110602.

37 X. Zhang, Y. Xiong, M. Dong and Z. Hou, *J. Electrochem. Soc.*, 2019, **166**, A2960–A2965.

38 A. Paulus, M. Hendrickx, M. Bercx, O. M. Karakulina, M. A. Kirsanova, D. Lamoen, J. Hadermann, A. M. Abakumov, M. K. Van Bael and A. Hardy, *Dalton Trans.*, 2020, **49**, 10486–10497.

39 Y. Wang, H.-T. Gu, J.-H. Song, Z.-H. Feng, X.-B. Zhou, Y.-N. Zhou, K. Wang and J.-Y. Xie, *J. Phys. Chem. C*, 2018, **122**, 27836–27842.

40 C. P. Laisa, R. N. Ramesha and K. Ramesha, *Electrochim. Acta*, 2017, **256**, 10–18.

41 Z. Tai, W. Zhu, M. Shi, Y. Xin, S. Guo, Y. Wu, Y. Chen and Y. Liu, *J. Colloid Interface Sci.*, 2020, **576**, 468–475.

42 Y. Tang, X. Han, W. Zhang and Y. He, *Ionics*, 2020, **26**, 3737–3747.

43 P. Zhang, X. Zhai, H. Huang, J. Zhou, X. Li, Y. He and Z. Guo, *Ceram. Int.*, 2020, **46**, 24723–24736.

44 A. Celeste, F. Girardi, L. Gigli, V. Pellegrini, L. Silvestri and S. Brutti, *Electrochim. Acta*, 2022, **428**, 140737.

45 J. Yang, Y. Chen, Y. Li, X. Xi, J. Zheng, Y. Zhu, Y. Xiong and S. Liu, *ACS Appl. Mater. Interfaces*, 2021, **13**, 25981–25992.

46 S. Maiti, H. Sclar, Rosy, J. Grinblat, M. Talianker, L. Burstein, M. Noked, B. Markovsky and D. Aurbach, *ACS Appl. Mater. Interfaces*, 2020, **12**, 32698–32711.

47 A. Ahuja, A. Kumar, A. Sengupta, M. Gautam, H. Lohani, P. Kumari and S. Mitra, *Energy Storage Mater.*, 2022, **52**, 169–179.

48 M. Chen, Y. Liu, Y. Zhang, G. Xing and Y. Tang, *Chem. Commun.*, 2022, **58**, 3591–3600.

49 B. Li, G. Rousse, L. Zhang, M. Avdeev, M. Deschamps, A. M. Abakumov and J.-M. Tarascon, *Energy Environ. Sci.*, 2023, **16**, 1210–1222.

50 P. Vahdatkhah, O. Voznyy and S. K. Sadrnezhaad, *Mater. Today Sustain.*, 2023, **21**, 100309.

51 H. Liu, C. Li, W. Tong and B. Hu, *J. Phys. Chem. Lett.*, 2023, **14**, 2323–2330.

52 J. Wu, H. Li, Y. Liu, Y. Ye and Y. Yang, *ACS Sustain. Chem. Eng.*, 2022, **10**, 6165–6180.

53 J. Sun, C. Sheng, X. Cao, P. Wang, P. He, H. Yang, Z. Chang, X. Yue and H. Zhou, *Adv. Funct. Mater.*, 2022, **32**, 2110295.

54 M.-J. Wang, A.-F. Shao, F.-D. Yu, G. Sun, D.-M. Gu and Z.-B. Wang, *ACS Sustain. Chem. Eng.*, 2019, **7**, 12825–12837.

55 F. Klein, J. Bansmann, Z. Jusys, C. Pfeifer, P. Scheitenberger, M. Mundszinger, D. Geiger, J. Biskupek, U. Kaiser, R. J. Behm, M. Lindén, M. Wohlfahrt-Mehrens and P. Axmann, *ChemSusChem*, 2022, **15**(20), e202201061.

56 W. Yu, Y. Wang, A. Wu, A. Li, Z. Qiu, X. Dong, C. Dong and H. Huang, *Green Energy Environ.*, 2024, **9**(1), 138–151.

57 X. Liu, C. Jiang, B. Yu, M. Wang, Y. Jin, Z. Fu, J. Chen, Z. Ma, B. Guo, Y. Huang, Z. Yang, R. Huang and X. Li, *Electrochim. Acta*, 2022, **418**, 140379.

58 D. Song, Z. Yang, Q. Zhao, X. Sun, Y. Wu, Y. Zhang, J. Gao, C. Wang, L. Yang, T. Ohsaka, F. Matsumoto and J. Wu, *ACS Appl. Mater. Interfaces*, 2022, **14**, 12264–12275.

59 J. Lan, Q. Zheng, H. Zhou, J. Li, L. Xing, K. Xu, W. Fan, L. Yu and W. Li, *ACS Appl. Mater. Interfaces*, 2019, **11**, 28841–28850.

60 Y. Meng, G. Chen, L. Shi, H. Liu and D. Zhang, *ACS Appl. Mater. Interfaces*, 2019, **11**, 45108–45117.

61 L. Wang, Y. Ma, Q. Li, Z. Zhou, X. Cheng, P. Zuo, C. Du, Y. Gao and G. Yin, *J. Power Sources*, 2017, **361**, 227–236.

62 B. Jiang, J. Li, B. Luo, Q. Yan, H. Li, L. Liu, L. Chu, Y. Li, Q. Zhang and M. Li, *J. Energy Chem.*, 2021, **60**, 564–571.

63 N. Srivastava, S. K. Singh, H. Gupta, D. Meghnani, R. Mishra, R. K. Tiwari, A. Patel, A. Tiwari and R. K. Singh, *J. Alloys Compd.*, 2020, **843**, 155615.

64 J. Zhao, X. Zhang, Y. Liang, Z. Han, S. Liu, W. Chu and H. Yu, *ACS Energy Lett.*, 2021, **6**, 2552–2564.

65 P. Hou, F. Li, H. Zhang and H. Huang, *J. Mater. Chem. A*, 2020, **8**, 14214–14222.

66 J. Yang, L. Xiao, W. He, J. Fan, Z. Chen, X. Ai, H. Yang and Y. Cao, *ACS Appl. Mater. Interfaces*, 2016, **8**, 18867–18877.

67 Z. Zhao, Z. Wen, C. Li, Y. Ding, Y. Jiang, F. Wu, B. Wu, S. Chen and D. Mu, *Electrochim. Acta*, 2020, **353**, 136518.

68 T. Kim, *Mater. Today Sustain.*, 2023, **21**, 100326.

69 Z. Wei, W. Zhang, F. Wang, Q. Zhang, B. Qiu, S. Han, Y. Xia, Y. Zhu and Z. Liu, *Chem.–Eur. J.*, 2015, **21**, 7503–7510.

70 R. Benedek, *J. Electrochem. Soc.*, 2022, **169**, 050505.

71 N. El Halya, M. Aqil, K. El Ouardi, A. Bano, A. El bendali, L. Hdidou, R. Amine, S.-B. Son, F. Ghamouss, D. T. Major, K. Amine, J. Alami and M. Dahbi, *Batter. Supercaps*, 2023, e202300424.

72 N. El Halya, K. Elouardi, A. Chari, A. El Bouari, J. Alami and M. Dahbi, in *Titanium Dioxide – Advances and Applications*, IntechOpen, 2022.

73 K. R. Prakasha, M. Sathish, P. Bera and A. S. Prakash, *ACS Omega*, 2017, **2**, 2308–2316.

74 S. Shi, T. Wang, M. Cao, J. Wang, M. Zhao and G. Yang, *ACS Appl. Mater. Interfaces*, 2016, **8**, 11476–11487.

75 J. Zeng, Y. Cui, D. Qu, Q. Zhang, J. Wu, X. Zhu, Z. Li and X. Zhang, *ACS Appl. Mater. Interfaces*, 2016, **8**, 26082–26090.

76 X. Cheng, H. Wei, W. Hao, H. Li, H. Si, S. An, W. Zhu, G. Jia and X. Qiu, *ChemSusChem*, 2019, **12**, 1162–1168.

77 C. P. Laisa, A. K. Nanda Kumar, S. Selva Chandrasekaran, P. Murugan, N. Lakshminarasimhan, R. Govindaraj and K. Ramesha, *J. Power Sources*, 2016, **324**, 462–474.

78 Y. Bai, Y. Li, C. Wu, J. Lu, H. Li, Z. Liu, Y. Zhong, S. Chen, C. Zhang, K. Amine and F. Wu, *Energy Technol.*, 2015, **3**, 843–850.

79 T. Zhao, N. Zhou, X. Zhang, Q. Xue, Y. Wang, M. Yang, L. Li and R. Chen, *ACS Omega*, 2017, **2**, 5601–5610.

80 T. Zhao, S. Chen, L. Li, X. Zhang, H. Wu, T. Wu, C.-J. Sun, R. Chen, F. Wu, J. Lu and K. Amine, *ACS Appl. Mater. Interfaces*, 2014, **6**, 22305–22315.

81 T. R. Penki, D. Shanmughasundaram and N. Munichandraiah, *Electrochim. Acta*, 2014, **143**, 152–160.

82 Y. Zhao, Y. Sun, Y. Yue, X. Hu and M. Xia, *Electrochim. Acta*, 2014, **130**, 66–75.

83 J. Karunawan, A. Sumboja and F. Iskandar, *AIP Conf. Proc.*, 2022, **1**, 2652.

84 S. Sallard, D. Sheptyakov and C. Villevieille, *J. Power Sources*, 2017, **359**, 27–36.

85 H. Ouyang, X. Li, Z. Wang, H. Guo, W. Peng and Z. He, *Funct. Mater. Lett.*, 2018, **11**, 1850083.

86 X. Bian, Q. Fu, X. Bie, P. Yang, H. Qiu, Q. Pang, G. Chen, F. Du and Y. Wei, *Electrochim. Acta*, 2015, **174**, 875–884.

87 D. Ostrovskii, F. Ronci, B. Scrosati and P. Jacobsson, *J. Power Sources*, 2001, **94**, 183–188.

88 Y. Bai, K. Jiang, S. Sun, Q. Wu, X. Lu and N. Wan, *Electrochim. Acta*, 2014, **134**, 347–354.